Simulating the Motion of Flexible Pulp Fibres Using the Immersed Boundary Method

John M. Stockie* and Sheldon I. Green†

*Department of Mathematics and Statistics, Simon Fraser University, Burnaby, British Columbia,
Canada V5A 1S6; †Department of Mechanical Engineering, University of British Columbia,
Vancouver, British Columbia, Canada V6T 1Z4
E-mail: jms@sfu.ca, green@mech.ubc.ca

The motion of flexible fibres suspended in an incompressible fluid is of interest to researchers in a wide variety of fields, including reinforced composite materials, biotechnology, and the pulp and paper industry. In this work, we concentrate on the application to pulp fibres and demonstrate how the complex hydrodynamic interaction between a flexible fibre and the surrounding fluid can be simulated using the *immersed boundary method*. The computations involve a single fibre suspended in a two-dimensional shear flow at moderate Reynolds number. Previous experimental work differentiates the observed fibre motions into a well-defined set of "orbit classes," which are reproduced in our simulations for fibres with varying flexibility. The computed fibre orientation angle distributions are compared to classical theoretical results and shown to exhibit a skewness which is not captured by either the linear theory or other recent numerical computations that ignore the fibre–fluid interaction. These simulations set the stage for further work in modeling flows with multiple fibres in three dimensions for the purpose of improving the papermaking process.   © 1998 Academic Press

Key Words: flexible fibres; pulp fibres; immersed boundary method; fluid–structure interaction.

1. INTRODUCTION

A thorough understanding of the behaviour of pulp fibres in suspension is extremely important to the pulp and paper industry in many stages of the papermaking process. The output of mechanical pulp refiners is a suspension of fibres of varying length and flexibility. Moderately flexible fibres are more desirable than rigid ones because they have larger relative bonding area and thus form paper with higher tensile strength and better printability [8] (inflexible fibres can be sent through a secondary refiner for enhancement of their flexibility). Hence, it is important to separate fibres based on their flexibility in order to produce high

147

quality paper. One method of performing this separation is to suspend the fibres in the shear flow generated by a pressure screen. A knowledge of the hydrodynamic behaviour of fibres with differing length and flexibility is essential to understanding the separation process.

A considerable amount of theoretical work has been done on modeling fibres, since fibre suspensions appear in many applications other than papermaking. Much of the theory centers around the motion of rigid cylindrical rods immersed in low Reynolds number or Stokes flows. Attempts have been made to add a small degree of flexibility, but these results are usually fairly limited in their application. Accordingly, much of the work on flexible fibres has been experimental, although more recently several numerical simulations have been undertaken.

The main purpose in this paper is to demonstrate that the complex interaction between a fibre and fluid can be handled using the *immersed boundary method*. This method was originally developed by Peskin [21] to simulate the flow of blood in the heart. It has since been applied to a diverse range of other applications involving swimming microorganisms [9], aggregation of blood platelets [10], biofilms [5], particle suspensions [11, 30], and plasma simulations [18]. The immersed boundary framework extends very naturally to handle flexible fibres in suspension, and we will show that the full range of observed planar fibre motions is reproduced in two-dimensional simulations.

The immersed boundary method's main advantages are its simplicity and geometric flexibility, which account in large part for its widespread use. It is a mixed Eulerian–Lagrangian scheme that combines the efficiency inherent in using a fixed Cartesian grid to compute the fluid motion, along with the ease of tracking the immersed boundary at a set of moving Lagrangian points. The key idea in this method is to replace the fluid–material interface with appropriate contributions to a force density term in the Navier–Stokes equations. The internal boundaries are thereby eliminated and a simple finite difference scheme can be used to solve the fluid equations, with the influence of the immersed boundary relegated to an inhomogeneous forcing term that is distributed onto fluid points that lie near the interface. The interface is modeled very simply using a data structure composed of "spring-like" links between adjacent points, which facilitates the handling of immersed boundaries of nearly arbitrary shape, size, and configuration.

We begin in the next section with an overview of the theoretical and experimental work that has been done on flexible pulp fibres, as well as more recent attempts to simulate their motion in computations. The mathematical framework used to model immersed fibres and the corresponding numerical method are described in Sections 3 and 4. We then present a series of pulp fibre simulations in Section 5 and draw comparisons with previous experiments and computations.

2. BACKGROUND: PULP FIBRES

2.1. *Theory and Experiments*

As early as 1922, Jeffery studied the motion of a single rigid, neutrally buoyant, elliptical particle in a homogeneous Stokes flow [17]. He proved that the center of the particle follows streamlines and that when subjected to a Couette flow it rotates about its center according to

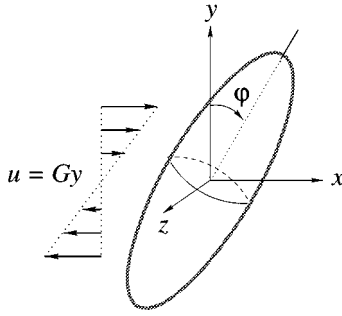$$\varphi(t) = \tan^{-1}\left[r_e \tan\left(\frac{Gr_e t}{r_e^2 + 1}\right)\right], \qquad (1)$$

FIG. 1.   Jeffery's ellipsoidal particle immersed in a linear shear flow.

where φ is the angle that the major axis of the ellipse makes with the vertical, G is the shear rate, and r_e is the ratio of the lengths of the major and minor axes of the ellipsoid (refer to Figs. 1 and 2).

Two things can be deduced from this formula: first, the particle has a nonuniform angular velocity which is largest when the particle's major axis is at right angles to the flow direction ($\varphi = 0°$) and drops to a minimum at $\varphi = 90°$; second, the period of motion is a constant, given by

$$T = \frac{2\pi}{G}\left(r_e + \frac{1}{r_e}\right),\tag{2}$$

which is approximately $T \approx 2\pi r_e/G$ for long, thin ellipsoids (when $r_e \gg 1$).

Wood pulp is not composed of these idealised ellipsoids, however, but rather hollow, cylindrical fibres of length 0.1 to 0.3 cm with aspect ratios ranging from 60 to 400. Anczurowski and Mason [1] showed that Jeffery's equation (1) could be used to describe the motion of rigid, cylindrical fibres by replacing r_e with an *equivalent ellipsoidal axis ratio* r_e^*, which is chosen by matching periods from experiments. Cox [4] found expressions for the force and torque on particles of various shapes in response to shear flow. He also derived an approximate formula for the equivalent aspect ratio for particles of various shapes, which compares very well with experiments.

While Jeffery's equation is a good approximation for rigid fibres, experiments establish that it cannot be applied to fibres that experience significant bending [19]. As a consequence,
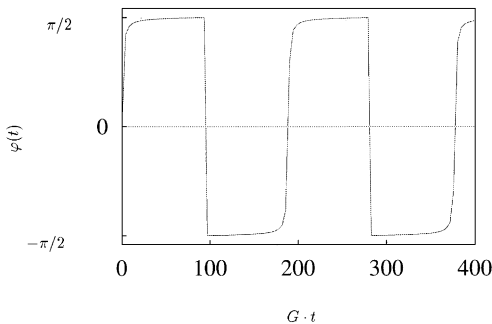

FIG. 2.   A plot of angular displacement of the rotating ellipsoid in the $x - y$ plane versus nondimensionalised time (for $r_e = 60$), predicted by theory.

TABLE I

Orbit Class		
I. Rigid rotation		↓
II. Springy rotation		
IIIA. Loop or S turn		
IIIB. Snake turn		↓
IV. Complex rotation		

(right column spanning label: decreasing stiffness / increasing length & shear rate)

much of the work on flexible fibres has focused on experimental observations of the periods and types of motion. Forgacs *et al.* [15] observed in experiments involving very dilute suspensions (with concentrations less than 0.01%) that fibres are essentially isolated and particle interactions can be neglected. When subjected to laminar shear, fibres tend to orient themselves in the direction of the shear flow, and when in motion they either rotate in very well-defined orbits, or bend in some predictable fashion. Experiments by Mason and co-workers [2, 19] identified a wide range of fibre behaviours, which they separated into distinct *orbit classes* based on the flexibility of the fibre. We have summarised the orbits which are two-dimensional in nature in Table I, since these are the only motions that can be simulated by our 2D fibre model (there are several other types of orbit involving *nonplanar motions*, such as spinning in the axial direction that we have not included here).

Rigid fibres (class I) rotate as solid cylinders, with angular velocity that reaches a maximum when the fibre is aligned at right angles to the direction of the shear flow. Flexible fibres have several possible modes of rotation, the simplest of which is called a *springy rotation* (class II), where the fibre still revolves but deforms into the shape of an arc during the spin. In the *loop* or *S-turn* (IIIA) and *snake turn* (IIIB), the fibre is deformed into a more intricate curved intermediate shape, after which it straightens out once again (the S-turn is rarely observed in experiments except for very carefully chosen initial configurations and a fibre with a high degree of symmetry [2]). The final class-IV orbit corresponds to a fibre that performs a snake-like turn but never straightens out, continuing to loop over itself; this is called a *complex rotation*. Forgacs *et al.* [15] used measurements of fibre flexibility to show that the various orbit classes occurred for different fibre stiffness values, with the stiffness decreasing as one moves down in the table. Differences also arise in orbital motion of fibres

when the shear rate and fibre length are varied, keeping the other physical parameters the same [14]. Fibre motion is thus a function of shear rate, bending stiffness, and fibre length.

2.2. *Computational Approaches*

The motion of flexible fibres in response to a shear flow can be quite intricate, and the analytical results cannot capture the full range of complexity of observed orbits. Furthermore, due to the small size of the fibres and the difficult and time-consuming process of accumulating accurate flow measurements, there are considerable restrictions placed on the information that can be culled from experiments. Hence, numerical simulations present an ideal opportunity to gain a deeper understanding of flexible fibre motion by studying the fine structure of fluid and fibre behaviour.

There have been several recent efforts to simulate fibre motion numerically. Yamamoto and Matsuoka [33] approximate a fibre as a chain of bonded spheres that are free to stretch, bend, and twist relative to each other. In this model, there is no hydrodynamic coupling between fluid and fibre: the fluid undergoes a given linear shear, and the motion of the fibre is determined by solving a set of dynamic equations with a given applied fluid force. Links between the spherical elements are governed by three stiffness constants (for stretching, bending, and twisting motions) whose values depend on the radii of the spheres and Young's modulus for the material. This work has since been extended to simulate large systems of particles [34] and also incorporates forces of attraction and repulsion between individual fibres.

Wherrett *et al.* [32] implemented a slightly modified version of the Yamamoto–Matsuoka model, which uses cylindrical elements instead of spheres. The stretching and bending stiffnesses are modified to include the aspect ratio of the elements, and the simulations are two-dimensional so that torsional motions are ignored. They derive a dimensionless *bending number*, which is used to relate the changes in computed periods of revolution to fibre flexibility. The work of Ross and Klingenberg [26] made use of another similar mechanical model, consisting of linked prolate spheroids. They eliminate axial stretching by linking the elements with *ball and socket joints*—real fibres do not stretch appreciably, even in highly sheared flows, and so this aspect of their model seems particularly advantageous.

Another class of method that has proven to be particularly well-suited for simulating many flows with complex geometry is the boundary element method. Ingber and Mondy [16] use this approach to study the motion of cylindrical particles in a Stokes flow, including the interactions with other particles and the channel walls.

In all of the work just mentioned, the influence of the fibres on the fluid has been neglected. Another approach has been to model fibres as simple rigid rods and concentrate instead on the hydrodynamic coupling between the fibres and the fluid. A rheological model for non-dilute fibre suspensions was used in [24, 25] to compute changes in the velocity field and relative viscosity of the fluid due to the presence of many fibres. However, this approach captures only the averaged properties of a large number of suspended particles, whereas the focus of our work is simulating the motion of individual fibres.

From the previous discussion, there is an obvious gap in the computational work on pulp fibres; namely, in the simulation of the hydrodynamic interaction between individual pulp fibres with the surrounding fluid. There is good agreement between theory and experiment for rigid fibres, and so it is unlikely that hydrodynamic coupling has a significant effect

in this case. However, the same cannot be said of flexible fibres, and it is here that the immersed boundary approach can make a substantial contribution.

3. MATHEMATICAL DESCRIPTION

Immersed fibres are flexible, force-bearing filaments, submerged within an incompressible fluid, that are assumed to be neutrally buoyant, massless, and to occupy zero volume. Three-dimensional immersed surfaces (such as the heart model of [22]) are composed of an interwoven mesh of such fibres. The typical assumptions made in analytical and numerical investigations of pulp fibres are that the fluid is Newtonian and incompressible and that the fibres are massless and neutrally buoyant. Furthermore, the flow conditions under which individual fibres are considered typically correspond to very low Reynolds numbers (typical fibre Reynolds numbers occurring in papermaking, based on the fibre diameter and slip velocity, are in the range 5–50 in a headbox slice and 2–10 in a twin wire former gap). Aspect ratios are very large, so that fibres are nearly one-dimensional structures. Taken together, these are precisely the assumptions made for immersed fibres, and so this model seems particularly well-suited to the representation of flexible pulp fibres. Under these conditions, the fibres themselves are incompressible, and the fluid–fibre system can be regarded as a composite, viscoelastic material. The main advantage to this model is that the fluid and fibre can be described by a single velocity field for which we now derive the equations of motion.

We consider a rectangular fluid domain, Ω, with dimensions $L_x \times L_y$, that is filled with an incompressible, viscous fluid, as pictured in Fig. 3. The top and bottom walls are moved with constant velocity U in opposite directions, resulting in a shear flow with shearing rate $G = 2U/L_y$. The boundary conditions are chosen to be periodic in the x-direction. Suspended within the fluid is a fibre, which can be described by a continuous curve Γ.

The motion of the fluid–fibre composite is governed by the incompressible Navier–Stokes equations,

$$\rho \frac{\partial \boldsymbol{u}}{\partial t} = -\rho \boldsymbol{u} \cdot \nabla \boldsymbol{u} + \mu \Delta \boldsymbol{u} - \nabla p + \boldsymbol{F}, \tag{3}$$

$$\nabla \cdot \boldsymbol{u} = 0, \tag{4}$$

where $\boldsymbol{u}(\boldsymbol{x}, t) = (u(\boldsymbol{x}, t), v(\boldsymbol{x}, t))$ is the fluid velocity, $p(\boldsymbol{x}, t)$ the pressure, $\boldsymbol{F}(\boldsymbol{x}, t)$ is the external force, and ρ and μ are the constant fluid density and viscosity. Let $\boldsymbol{x} = X(s, t)$ represent the position of the fibre, where s is a parameterisation of Γ in some reference configuration (typically, s is taken to be the arclength of the fibre in an unstressed state, although as the fibre evolves in time s will not necessarily be a measure of arclength).
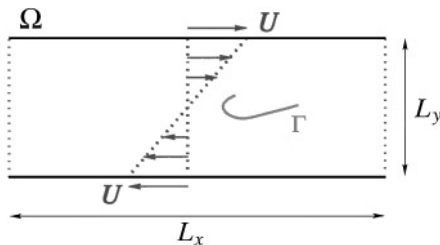

FIG. 3. The periodic channel domain for the pulp fibre simulations, with shearing motion induced by moving top and bottom walls.

Gravitational effects can be assumed negligible because the fibre is neutrally buoyant, which implies that the external force $\boldsymbol{F}$ arises solely from the action of the elastic fibre. The force is zero everywhere except on the fibre, and so the fluid body force $\boldsymbol{F}$ is a distribution and can be written compactly as the convolution of a fibre force density, $\boldsymbol{f}(s, t)$, with a delta function,

$$F(\boldsymbol{x}, t) = \int_{\Gamma} \boldsymbol{f}(s, t) \cdot \delta(\boldsymbol{x} - \boldsymbol{X}(s, t)) \, ds, \tag{5}$$

where $\delta(\boldsymbol{x}) = \delta(x) \cdot \delta(y)$ is the product of two Dirac delta functions. The immersed fibre is required to move at the same velocity as neighbouring fluid particles, and so we write

$$\frac{\partial \boldsymbol{X}}{\partial t} = \boldsymbol{u}(\boldsymbol{X}(s, t), t),$$

$$= \int_{\Omega} \boldsymbol{u}(\boldsymbol{x}, t) \cdot \delta(\boldsymbol{x} - \boldsymbol{X}(s, t)) \, d\boldsymbol{x}, \tag{6}$$

where this second delta-function form of (6) is used to great advantage in the immersed boundary method, which we describe in the next section.

The final component needed to close the system of Eqs. (3)–(6) is an expression for the force per unit length, $\boldsymbol{f}(s, t)$, along the fibre. In the immersed boundary method, the fibre is tracked at a discrete set of N_b points, $\boldsymbol{X}_\ell$, for $\ell = 1, 2, \ldots, N_b$, which move in time. The force density at any point is a function of the fibre configuration, which for wood pulp must take into account the resistance of the individual fibres to stretching/compression and bending. We take an approach that follows that used for immersed boundary computations of swimming marine worms [9], wherein the force is modeled by means of a set of force-bearing "links" between nearby points on the fibre. The fibre force density at a given point, $\boldsymbol{f}_\ell$, is written as the gradient of a potential function $E(\ldots, \boldsymbol{X}_\ell, \boldsymbol{X}_{\ell+1}, \ldots)$:

$$\boldsymbol{f}_\ell = -\frac{\partial E}{\partial \boldsymbol{X}_\ell}. \tag{7a}$$

Contributions to the force arising from stretching-resistant links between successive fibre points can be considered as arising from the potential

$$E_s = \frac{1}{2} \sum_{\ell=0}^{N_b-1} \sigma_s (\|\boldsymbol{X}_{\ell+1} - \boldsymbol{X}_\ell\| - r_o)^2, \tag{7b}$$

where σ_s is the stretching stiffness and r_o is the resting length of the link joining each pair of points. Each term in the sum represents a spring-like link between two neighbouring points on the fibre. This can be seen by differentiating the sum at $\boldsymbol{X}_\ell$, which leads to two contributions to the force density in (7a) of the form

$$\sigma_s (\|\boldsymbol{X}_{\ell+1} - \boldsymbol{X}_\ell\| - r_o) \frac{(\boldsymbol{X}_{\ell+1} - \boldsymbol{X}_\ell)}{\|\boldsymbol{X}_{\ell+1} - \boldsymbol{X}_\ell\|};$$

the second involving points $\boldsymbol{X}_\ell$ and $\boldsymbol{X}_{\ell-1}$. Written in this manner, the force is clearly like that of a spring obeying Hooke's law, with resting length r_o and stiffness σ_s, directed along the vector joining $\boldsymbol{X}_\ell$ and $\boldsymbol{X}_{\ell+1}$. Figure 4a pictures a link of this type and the forces arising at each of the two points involved.
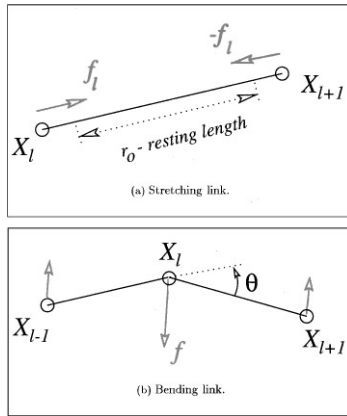
FIG. 4. Two types of links are used to model flexible fibres: stretching/compression-resistant links between pairs of points; and bending–resistant links between triplets of points.

The bending-resistant links, on the other hand, can be incorporated using a force that drives the angle between successive triplets of points to a given *equilibrium angle* θ_0. An energy function that accomplishes this is

$$\mathcal{E}_b = \frac{1}{2} \sum_{\ell=1}^{N_b-1} \sigma_b \left[\hat{z} \cdot (X_\ell - X_{\ell-1}) \times (X_{\ell+1} - X_\ell) - r_o^2 \sin \theta_o \right]^2, \tag{7c}$$

where $\hat{z} = (0, 0, 1)$ and $r_o^2 \sin \theta_o$ is related to the *equilibrium curvature* of the fibre (it is actually the quantity $\sin \theta_o / r_o$ that has the interpretation of curvature—see [9, pp. 90–92] for a full discussion). To model a straight rod, we select $\theta_o = 0$ for each link. The term enclosed in square brackets in Eq. (7c) may be rewritten as

$$\|X_\ell - X_{\ell-1}\| \cdot \|X_{\ell+1} - X_\ell\| \sin \theta - r_o^2 \sin \theta_o,$$

which is approximately $r_o^2 (\theta - \theta_o)$ when the fibre is close to equilibrium; hence, this contribution to the energy function serves to drive the angle between neighbouring pairs of links to θ_o.

The energy function describing a flexible fibre is now given by

$$\mathcal{E} = \mathcal{E}_s + \mathcal{E}_b. \tag{7d}$$

The stretching and bending forces given in (7b) and (7c) are very similar to that used in the mechanical pulp fibre models mentioned earlier in Section 2.2. The main difference here is that in the immersed boundary model, the fibre force actually influences the flow of the surrounding fluid.

4. NUMERICAL METHOD

The immersed boundary method (discussed briefly in the Introduction) is a mixed Eulerian–Lagrangian finite difference scheme for computing the motion of immersed fibres. The fluid variables are defined on a fixed, Eulerian, $N_x \times N_y$ grid of points, with positions $x_{i,j} = (x_i, y_j) = (ih, jh)$ for $i = 1, \ldots, N_x$ and $j = 1, \ldots, N_y$. The values of N_x and N_y are
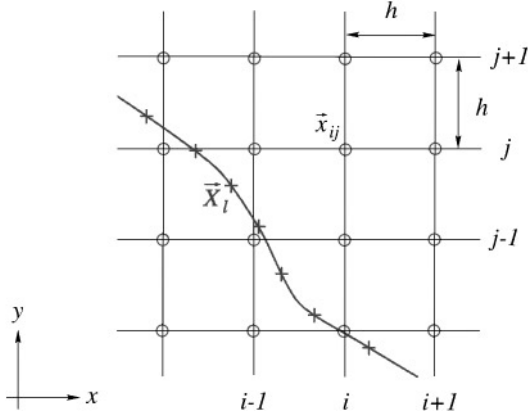
FIG. 5. The relationship between fluid (◯) and fibre (+) grid points.

chosen so that the mesh spacing $h = L_x/N_x = L_y/N_y$ is equal in both directions. The fluid domain is periodic in the x-direction, so that the points x_0 and x_{N_x} are identified with each other. The fibre position, on the other hand, is a Lagrangian quantity which is discretised as a set of N_b moving points, so that the parameter s is taken at discrete locations $s_\ell = \ell \cdot h_b$, where $h_b = L_f/N_b$ and L_f is the length of the fibre. Both fluid and fibre quantities are sampled at equally spaced times $t_n = n \cdot k$, where k is the time step. Figure 5 depicts a typical fluid–fibre grid.

The delta functions appearing in Eqs. (5) and (6) are replaced by a discrete approximation $\delta_h(\boldsymbol{x})$, which is the product of 2 one-dimensional discrete delta functions,

$$\delta_h(x_i, y_j) = d_h(x_i) \cdot d_h(y_j). \tag{8a}$$

The choice of d_h typically used in immersed boundary computations is

$$d_h(r) = \begin{cases} \frac{1}{4h}\left(1 + \cos\frac{\pi r}{2h}\right), & \text{if } |r| < 2h, \\ 0, & \text{if } |r| \geq 2h. \end{cases} \tag{8b}$$

It will become clear in the algorithm to follow that $\delta_h(\boldsymbol{x})$ acts to interpolate quantities between the fluid and fibre grid points.

We are now in a position to describe the immersed boundary algorithm, which is a procedure for taking the fluid velocity and fibre position ($\boldsymbol{u}_{i,j}^n$ and $\boldsymbol{X}_{i,j}^n$) at time t_n and evolving them to time level $n+1$:

Begin. $n = 0$.
Step 1. Calculate the force density $\boldsymbol{f}_\ell^n$ at fibre points using Eqs. (7a)–(7d).
Step 2. Distribute the force density onto nearby fluid grid points using the discrete form of (5) with the delta function given by (8a) and (8b):

$$\boldsymbol{F}_{i,j}^n = \sum_{\ell=1}^{N_b} \boldsymbol{f}_\ell^n \cdot \delta_h\left(\boldsymbol{x}_{i,j} - \boldsymbol{X}_\ell^n\right) \cdot h_b.$$

Step 3. Solve the Navier–Stokes equations (3)–(4) for the velocity at the next time step, $\boldsymbol{u}_{i,j}^{n+1}$, using Chorin's projection scheme [3]. This method is a three-step process in which:

1. convection and diffusion are applied implicitly to obtain an "intermediate" velocity;
2. a Poisson equation is solved for the pressure; and
3. the pressure is used to update the intermediate velocity so that it is divergence-free.

Step 4. The resulting fluid velocity, $u_{i,j}^{n+1}$, is interpolated onto neighbouring fibre points and the fibre is evolved in time:

$$X_\ell^{n+1} = X_\ell^n + k \cdot \sum_{i,j} u_{i,j}^{n+1} \cdot \delta(x_{i,j} - X_\ell^n) \cdot h^2.$$

Repeat. $n \mapsto n + 1$.

The algorithm is described in full detail in [23].

If we restrict the dimensions of the domain so that N_x is an integer power of 2, then a fast Fourier transform (FFT) algorithm may be applied to solve the pressure Poisson equation in Step 3. The channel domain is periodic in x and so an FFT is performed in the x-direction only, in contrast with most other immersed boundary computations in which the fluid domain is taken to be doubly periodic. After transforming the equations, there remains a banded linear system to be solved for the transformed variables in the y-direction. The pressure is then found by transforming back to real variables by an inverse FFT. The boundary conditions on velocity and pressure are periodic in the x-direction and the velocities along the top and bottom walls are prescribed so as to give the required shear rate. The difference stencil for the pressure at points on or adjacent to the channel walls is modified using Chorin's projection scheme, which is described in detail along with the channel FFT solver in [28, Appendix].

5. COMPUTATIONAL RESULTS

Our main purpose in this paper is to demonstrate that the immersed boundary method is a useful tool for simulating the motion of pulp fibres. To this end, we present comparisons with experimental and theoretical results—both qualitative and quantitative—to illustrate that the computed results capture the important physics of pulp fibre motion. Before presenting the simulations, we give a brief summary of the physical parameters relevant to pulp fibre motion and their typical values.

5.1. *Physical Parameters*

Experiments are often performed on synthetic fibres made of rayon or dacron, immersed in highly viscous fluids such as corn syrup or castor oil [14]. Representative values of parameters in experiments are listed in Table II, with references to the literature where appropriate.

While the physical parameters corresponding to some experiments differ significantly from those for actual pulp fibres, the observed behaviour is very similar. Therefore, we will perform simulations on parameters for both situations whenever possible in order to cover as wide a range of physics as we can, within the stability constraints set by the numerical scheme. The range of parameters under consideration here correspond to flows with relatively high viscosity and moderate shear rates, so that the Reynolds numbers lie in

TABLE II

Parameter	Values	Units	References
ρ (density)	1.0	g/cm^3	
μ (viscosity)	10–90 (castor oil/corn syrup)	g/cm $\cdot$ s	[13, 14]
	0.01 (water)		
G (shear rate)	1–100 (experiment)	s^{-1}	[13, 14]
EI (bending stiffness)	0.001–0.07 (paper pulp)	g cm^3/s^2	[7, 8, 27]
	0.6 (nylon)		
L_f (fibre length)	0.1–0.3	cm	[7, 32, 13]
r_c (aspect ratio)	10–60 (natural)	—	[32]
	40–400 (synthetic)		[13, 14]
Re (Reynolds number)	0.01–50	—	

the range Re $\lesssim 50$. Although the immersed boundary method is well known to suffer from severe time step restrictions at high Reynolds numbers [20], this range of Re is well within what is considered normal in immersed boundary computations.

Our computational test chamber was taken to be a rectangle of dimensions 2 cm $\times \frac{1}{2}$ cm, within which was suspended a fibre of length 0.1–0.2 cm. We concentrate mainly on the effects of shear rate (which has typically been the variable quantity in experiments) and bending stiffness, since both can be changed easily without modifying the computational domain. The problem was discretised with a mesh spacing of $h = \frac{1}{64}$ cm (i.e., 128×32 fluid grid points) and either 40 or 80 fibre points, depending on whether the fibre is 0.1 or 0.2 cm long. The mesh spacing and domain size were chosen so as to minimise the effect of boundaries on the solution, while at the same time keeping computational cost to a minimum. We performed a series of tests with various channel aspect ratios to show that for $h = \frac{1}{64}$, the domain could be taken as small as $2 \times \frac{1}{2}$ without appreciably changing the qualitative behaviour of the computed solution, where the fibre length ranged from 0.1 to 0.2 cm.

The time step k required for stability lies the range 2.0–5.0 $\times 10^{-5}$. The bending stress parameter σ_b has the same interpretation as Young's modulus E; this quantity is chosen so that when scaled by an appropriate moment of area, I, the resulting product $E \cdot I$ lies in the range 0.001–1.0 g cm^3/s^2. There is no physical equivalent for the stretching stiffness σ_s, since pulp fibres do not stretch appreciably; consequently, we chose a value large enough (typically from 5000–10000 g/cm$^3 \cdot$ s^2) so that the fibre length was held to within 2% of its initial value throughout most simulations.

It will prove particularly useful for us in our comparison of computations with experiments to consider a nondimensional parameter, which is a measure of fibre flexibility. We mentioned in Section 2.1 that the deformation of an individual fibre is a function of the fibre length and stiffness and the fluid shear rate. Using a dimensional analysis argument, it is possible to show [28] that the flow-induced bending of a flexible fibre is governed by a single, dimensionless parameter,

$$\chi = \frac{\mu G L^3}{EI}, \tag{9}$$

which depends on these three quantities, in addition to the fluid viscosity. The derivation of

χ depends on the drag coefficient, which has markedly different behaviour at low and high Reynolds number. As a result, Eq. (9) is derived assuming low Re or *creeping flows*, which are typical of the fibres under consideration here (although alternate expressions are given in [28] for the cases of high Re and three-dimensional flows). It is interesting to note that the fibre aspect ratio does not appear in the parameter χ, which is a consequence of the fact that fibre thickness does not play a role in the behaviour of fibres in two-dimensional flows. In 3D, on the other hand, the dimensional analysis leads to a flexibility parameter χ having an additional factor of D, the fibre diameter (see [28]), and hence, it is natural to expect that a three-dimensional model will have to include the effect of the fibre aspect ratio.

The parameter (9) has appeared before as a *dimensionless shear rate* in [26], and its reciprocal as a *bending number* in [32]. The latter work utilised the bending number to compare qualitative behaviour of fibres, and we will draw a similar comparison for the situation where hydrodynamic interactions between fluid and fibre are included. The quantity χ will be used in the pulp fibre simulations in the next section to separate between the various regimes of fibre motion.

5.2. *Simulations*

We begin by comparing the qualitative behaviour of solutions for four choices of bending stiffness that reproduce the orbit classes pictured earlier in Table I. Time sequences from the simulations are given in Fig. 6 for EI lying between 0.006 and 0.5.

The other parameters were chosen to be $G = 10$, $L = 0.1$, and $k = 5 \times 10^{-5}$, except for the first set of images where the stretching stiffness restricted the time step to half that size. The fibre was initially given a small curvature and inclined at a slight angle to the flow, so that the various orbits would develop within a reasonable amount of time.

By comparing the images up to time $t = 0.09$ s, we can see that the flexible fibres complete their first half-rotation in a significantly shorter time than the rigid fibre. This behaviour has been observed in experiments [2]. Something which is not apparent from these images is that, after completing the loop, the fibres in the first three orbits spend a great deal of time near the horizontal. This is consistent with the theoretical orbits for rigid fibres given by Jeffery's equation (1); plots of the orientation angle (the angle between the vertical and the straight line joining the endpoints of the fibre) versus time look very similar to that pictured in Fig. 2 for rigid ellipsoids. The fourth fibre never straightens out, and hence, its classification as a "complex rotation"—the period of rotation is significantly smaller and the fibre begins another turn very shortly after $t = 0.15$ s. The other fibres eventually pass through $\varphi = 90°$ as well and begin a second loop that is essentially identical to the first, with the period of rotation decreasing as the fibre stiffness decreases.

We can draw a more quantitative comparison with the theoretical predictions in terms of the amount of time the fibre spends at each angle φ. We ran another series of computations with bending stiffness fixed at $EI = 0.01$ and the shear rate taken between 50 and 80 for which all fibres underwent snake turns. The orientation angle was measured relative to the line joining the endpoints of the fibre, and we computed for a period of time comprising at least four complete rotations. The probability distribution of φ, which was estimated from the computed results, is plotted in Fig. 7 at open points. Given a set of observed orientation angles φ^n at discrete times t_n for $n = 1, 2, \ldots, M$, then the probability that φ lies between the two angles φ_o and $\varphi_o + \Delta$ (with Δ chosen "small enough" for plotting purposes) was
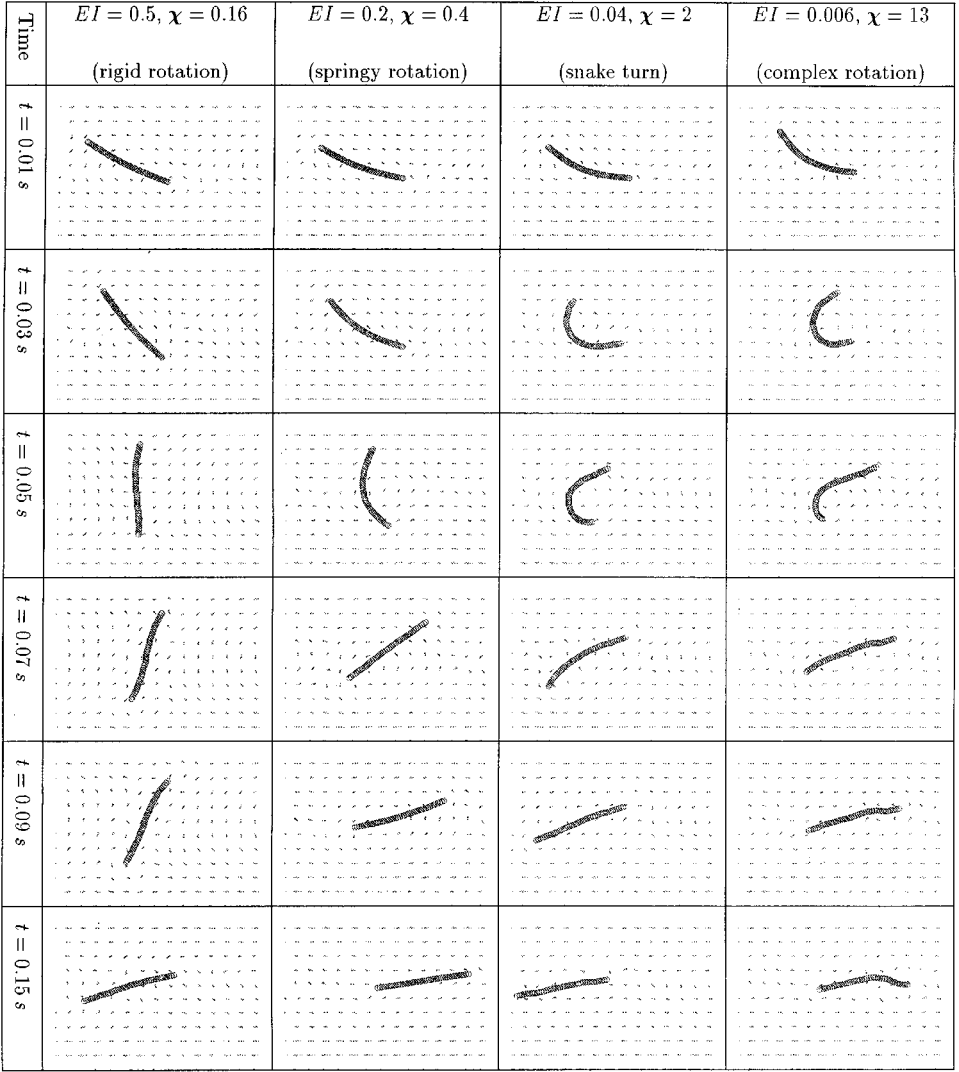
FIG. 6. Time sequences of orbits at time 0.01, 0.03, 0.05, 0.07, 0.09, and 0.15.

estimated using the formula

$$\text{Prob}(\varphi \in [\varphi_o, \varphi_o + \Delta]) \approx \frac{\#\{\varphi^n \in [\varphi_o, \varphi_o + \Delta]\}}{M}.$$

Figure 7 also contains the corresponding distributions of φ from Eq. (1) plotted as dotted curves. These theoretical predictions are computed in a similar manner by choosing an equivalent ellipsoidal axis ratio, r_e^*, that corresponds to the average period observed for each of the computed orbits.

From the computational results, it is clear that the fibre spends the majority of its time near the horizontal, which is consistent with the theory. Disregarding the slight offset of the curve near the peak, both the size and shape of the computed distribution is comparable to the prediction from Jeffery's equation.
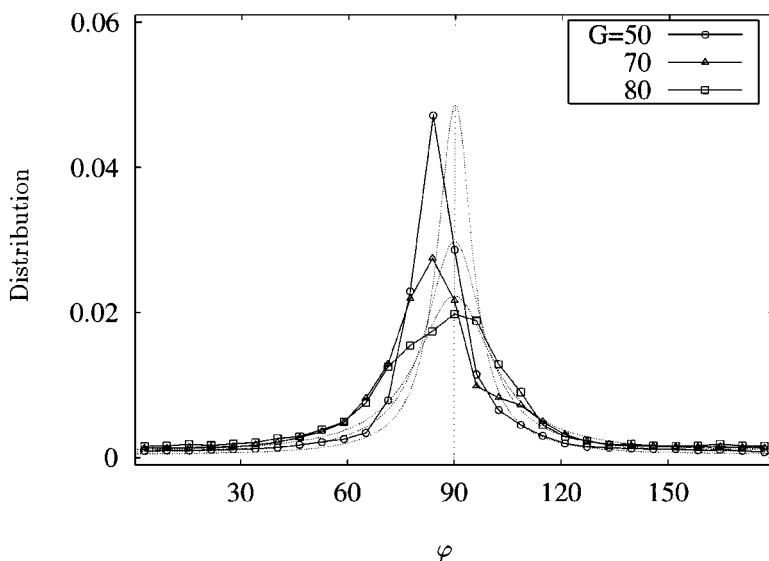
FIG. 7.   Distribution of time spent at various angles throughout the motion of a fibre undergoing springy rotation. The shear rate is varied from 50 to 80. The solid curves with points represent the computed orientation angles. The dotted curves are the corresponding theoretical predictions from Jeffery's equation (1) (the axis ratio is not defined for our linear fibre, and so we have chosen an r_e^* that gives a Jeffery period equal to the average period in our simulations for each value of G).

However, unlike the theoretical and computational results for rigid fibres and simulations of flexible fibres that ignore hydrodynamic interactions (such as [33, Fig. 10]), the distribution *is not symmetric about $\varphi = 90°$*. Rather, there is a tendency for the fibre to remain at an angle slightly above the horizontal plane. This asymmetry can be measured by the fraction of the area under the distribution curve that lies to the left of the $\varphi = 90°$ line, which is 0.70, 0.65, or 0.54, corresponding to whether the flow has shear rate $G = 50$, 70, or 80, respectively. We claim that the departure from the value of 0.50 for a Jeffery orbit is due to the interaction between fibre and fluid, which is not included in either previous computations or the analytical formulae. Although the fibre remains approximately flat when stalled in the stream-wise direction, it undergoes small flexing motions that cause the streamlines to curve slightly upward into the upper half of the channel before the fibre reaches $\varphi = 90°$ (see Fig. 8). This appears to be enough to cause the slight skewness in angle distribution
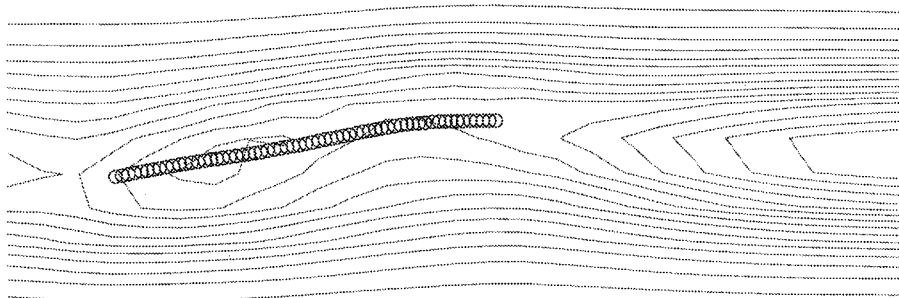

FIG. 8.   Flow streamlines for a fibre stalled at an angle $\varphi > 0$. The streamlines are deformed near the fibre, and there are narrow zones of recirculation to the front and rear. Note that even though the instantaneous streamlines cross the fibre, no fluid flows passes through since the fibre is moving with the fluid.

observed here and is something that we observe in all simulations over a wide range of parameter values.

This skewness in the φ-distribution has been observed in both experiments [29] and numerical simulations [31] involving semi-dilute suspensions—an effect that becomes more pronounced as the concentration of fibres is increased. In [12], a theoretical model for handling fibre–fibre interactions is developed, and the authors suggest that the anisotropy is due to normal stresses in steady shear flow that have also been observed in experiments. Our numerical simulations demonstrate that a similar phenomenon also occurs when the influence of an individual fibre on the surrounding fluid is taken into account, something which to our knowledge has not been considered before. Due to the periodic boundary conditions applied on the channel ends, we are actually computing the behaviour of a periodic array of fibres. Increasing the channel length by a factor of 2 (keeping the fibre length constant) has no noticeable effect on the qualitative behaviour of the fibre orbits, and so we expect the results to be nearly identical for single fibres as well.

We have also performed a grid refinement study to demonstrate that the orbital motions just described are insensitive to the choice of spatial mesh. This is particularly important in our computations, since the interpolation function for the fibre force lends an artificial "thickness" to the fibre. In long-time integrations, the spatial errors in the scheme accumulate to such a degree that a convergence study based on the fluid velocity or fibre position would not yield any meaningful information. However, the qualitative features of fibre orbits, such as the orientation angle distribution or fibre shape can be easily compared. When the number of fluid grid points is taken to be $N = 64$, 128, or 256 (and N_b is correspondingly doubled), the fibre orbits and streamline patterns shown in Figs. 6 and 8 remain essentially the same. Even for longer simulations over a large number of fibre orbits, the qualitative features of the solution, such as the orientation angle distribution, are unchanged. Figure 9 depicts the distribution curve for the $G = 80$ simulation pictured earlier in Fig. 7, from which it is clear that there is no significant change in the time spent at various angles when the grid is refined
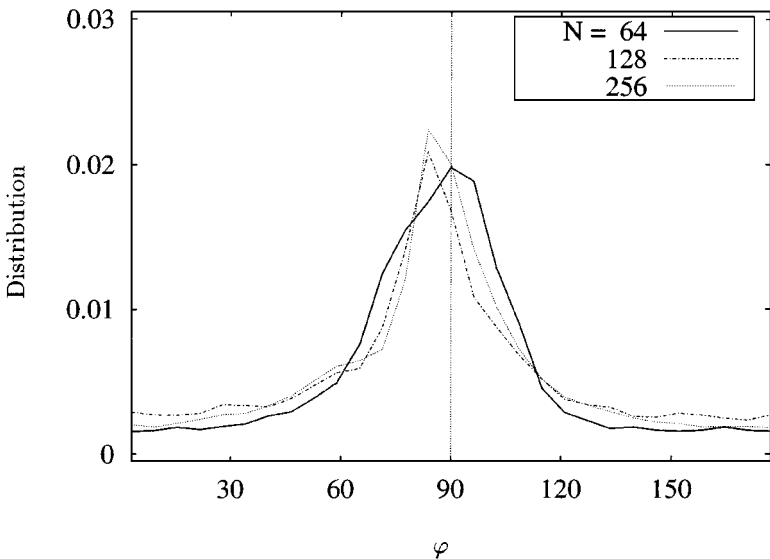

FIG. 9.   Orientation angle distribution for the $G = 80$ simulation pictured in Fig. 7, with the number of grid points N chosen to be 64, 128, or 256 (with $N_b = 40$, 80, or 160).
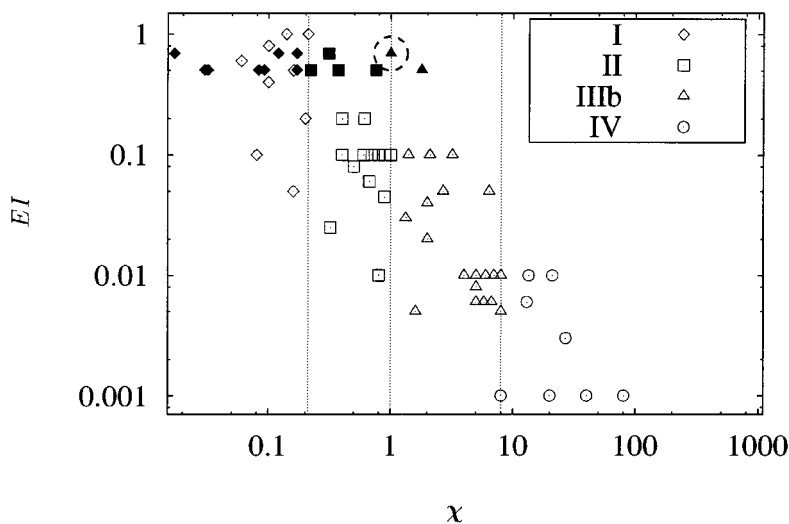
FIG. 10. Comparison of the orbit class with bending stiffness and χ. The fibre length, shear rate, and viscosity are also varied, which accounts for the spread of the data from a straight line. The computed orbits are plotted with open points; experiments from [14, Table III] are plotted as solid points for comparison.

by a factor of two. The skewness measures for the three cases are 0.54, 0.58, and 0.57 as N increases from 64 to 256. Similar results are also observed for the other values of shear rate.

Owing to the large amount of experimental data available in the literature, it is a fairly easy task to compare our computations with observations of actual fibres, particularly with the aid of the nondimensional parameter χ. To this end, we have run a large number of simulations with varying fibre length, bending stiffness, shear rate, and viscosity. The resulting orbit classifications have been plotted in Fig. 10 in terms of the nondimensional flexibility measure χ and the bending stiffness EI. Each computed orbit was classified as belonging to either class I, II, IIIB, or IV, using a different shape of open point for each (class IIIA was never observed in the computations). Our criterion for judging the orbit class was based on the *exterior angle*, α, between the tangent lines at the endpoints of the fibre (see Fig. 11):

I. If $175° < \alpha < 180°$, then the fibre was considered rigid.

II. For $90° < \alpha < 175°$, the ends of the fibre always deformed in unison to induce a springy rotation.

IIIB. When $\alpha < 90°$, the ends of the fibre tended to move independently of each other, leading to a snake turn. This independence of the motion of fibre ends was the same criterion used in [14] to identify snake turns, although the observation that the division occurred at an angle of approximately $90°$ was not.

IV. When the fibre never straightened out, the orbit was classified as a complex rotation.

FIG. 11. Definition of the exterior angle α, measured between the ends of a flexible fibre.

There is a clear division of the orbit classes, which have been drawn as vertical lines at values of $\chi \approx 0.25$, 1.0, and 8. This is very strong evidence of our premise that χ is a useful measure of fibre flexibility.

To push the comparison even further, we have included on the same set of axes a sequence of solid points which were taken from experiments by Forgacs and Mason [14], performed with dacron and rayon filaments suspended in corn syrup or castor oil. In order to ensure that the scaling between experimental and computational results is the same, we have adjusted the parameter χ based on a single experimental data point (circled in Fig. 10), which was classified as lying on the borderline between a springy rotation and a snake turn: the value of χ was set to equal 1.0 for this experiment, and all other experimental points were scaled by the same factor. The line $\chi = 0.25$ captures the division of experimental values between rigid and springy orbits very sharply, and so it appears that the computational model predicts quite well the qualitative behaviour of fibre orbits observed in experiments.

These results verify that the immersed boundary method can indeed be used to simulate the motion of flexible fibres at low Reynolds number. The qualitative behaviour of fibre orbits is very similar to what is observed in experiments, both in terms of the orbit classification and the distribution of angular displacement throughout the orbital period.

6. CONCLUSIONS

In this work, we have introduced a new application of the immersed boundary method to simulating the flow of pulp fibres in two dimensions. This work is of particular interest to the papermaking industry, as it is one of the first attempts to compute the hydrodynamic coupling between a flexible fibre and an incompressible fluid. We demonstrate that the method reproduces the tumbling motions of fibres observed experimentally in shear flows for reasonable physical parameters. Comparisons of the fibre orientation angle distribution with theoretical predictions and experimental observations are also in very close agreement. We also show that the immersed boundary model is able to capture the influence of the fibre on the fluid, which is manifested as a tendency for pulp fibres suspended in a horizontal shear flow to remain inclined at angles slightly above the shear direction—a phenomenon not seen either in other simulations or theory that ignores the fluid–fibre interaction. As a consequence, the immersed boundary method consequently shows considerable promise as a qualitative tool in pulp fibre modeling.

While we have restricted ourselves to two-dimensional simulations of isolated pulp fibres and comparisons to planar fibre motions, the immersed boundary method also has great potential for future applications in many other aspects of fibre motion. We have so far ignored several other orbit classes that are fundamentally three-dimensional and other important 3D effects such as the ability of fluid to flow easily around the sides of a thread-like fibre. We plan to extend our method to 3D in the near future, using a "bundle" of interwoven immersed fibres to represent a flexible fibre with finite thickness. This is essential in 3D flows, where the fibre aspect ratio plays an important role.

We also plan to include the effects of interactions between individual fibres in semi-dilute pulp suspensions where aggregation of fibres, or *flocculation*, is an important factor. By including both fibre–fibre and fibre–fluid forces, we hope to be able to go further in accurately predicting the motion of fibres in suspension. Extensive immersed boundary computations of multiparticle systems have already been performed by Peskin and Fogelson [11], who remarked that they could perform simulations of 1000 or so particles in two dimensions,

with the advantage of the immersed boundary method being that the computational work increases only *linearly* with the number of particles. These authors incorporate particle–particle interactions using appropriate modifications to the force in the fluid equations, which we plan to conform with the physics of pulp fibre interaction using the previous work on aggregation of slender particles [6, 34]. By incorporating the third dimension and interparticle forces, we can significantly increase the range of flow phenomena that can be investigated using the immersed boundary method in the papermaking process.

Our pulp fibre simulations to this point have neglected fibre inertia, which plays a significant role in some situations, such as separation of fibres in a hydrocyclone. Massive particles can be accounted for in the immersed boundary model by including a variable density in the momentum equations, as described in [23]. Each fibre contributes a singular mass distribution to the fluid of the form

$$\rho(\boldsymbol{x}, t) = \rho_o + \int_\Gamma m(s) \cdot \delta(\boldsymbol{x} - \boldsymbol{X}(s, t)) \, ds,$$

where $m(s)$ is the *additional mass per unit length* of the fibre (which can be negative), and ρ_o is the constant fluid density in the absence of the fibres. A variable density precludes the use of an FFT solver for the pressure, and so this extension will require development of an alternate fast fluid solver.

REFERENCES

1. E. Anczurowski and S. G. Mason, The kinetics of flowing dispersions. II. Equilibrium orientations of rods and discs (experimental), *J. Colloid Interface Sci.* **23**, 533 (1967).

2. A. P. Arlov, O. L. Forgacs, and S. G. Mason, Particle motions in sheared suspensions. IV. General behaviour of wood pulp fibres, *Svensk Papperstidn.* **61**(3), 61 (1958).

3. A. J. Chorin, Numerical solution of the Navier–Stokes equations, *Math. Comp.* **22**, 745 (1968).

4. R. G. Cox, The motion of long slender bodies in a viscous fluid. Part 2. Shear flow, *J. Fluid Mech.* **45**(4), 625 (1971).

5. R. Dillon, L. J. Fauci, A. L. Fogelson, and D. Gaver III, Modeling biofilm processes using the immersed boundary method, *J. Comput. Phys.* **129**(1), 57 (1996).

6. M. Doi and D. Chen, Simulation of aggregating colloids in shear flow, *J. Chem. Phys.* **90**(10), 5271 (1989).

7. P. A. T. Doo and R. J. Kerekes, A method to measure wet fiber flexibility, *Tappi J.* **64**(3), 113 (1981).

8. P. A. T. Doo and R. J. Kerekes, The flexibility of wet pulp fibres, *Pulp Paper Canada* **83**(2), 46 (1982).

9. L. J. Fauci and C. S. Peskin, A computational model of aquatic animal locomotion, *J. Comput. Phys.* **77**, 85 (1988).

10. A. L. Fogelson, A mathematical model and numerical method for studying platelet adhesion and aggregation during blood clotting, *J. Comput. Phys.* **56**, 111 (1984).

11. A. L. Fogelson and C. S. Peskin, A fast numerical method for solving the three-dimensional Stokes' equations in the presence of suspended particles, *J. Comput. Phys.* **79**, 50 (1988).

12. F. Folgar and C. L. Tucker III, Orientation behavior of fibers in concentrated suspensions, *J. Reinf. Plastics Compos.* **3**, 98 (1984).

13. O. L. Forgacs and S. G. Mason, Particle motions in sheared suspensions. IX. Spin and deformation of threadlike particles, *J. Colloid Interface Sci.* **14**, 457 (1959).

14. O. L. Forgacs and S. G. Mason, Particle motions in sheared suspensions. X. Orbits of flexible threadlike particles, *J. Colloid Interface Sci.* **14**, 473 (1959).

15. O. L. Forgacs, A. A. Robertson, and S. G. Mason, The hydrodynamic behaviour of paper-making fibres, *Pulp Paper Mag. Canada* **59**(5), 117 (1958).

16. M. S. Ingber and L. A. Mondy, A numerical study of three-dimensional Jeffery orbits in shear flow, *J. Rheol.* **38**(6), 1829 (1994).

17. G. B. Jeffery, The motion of ellipsoidal particles immersed in a viscous fluid, *Proc. R. Soc. A* **102**, 161 (1922).

18. G. Lapenta, F. Iinoya, and J. U. Brackbill, Particle-in-cell simulation of glow discharges in complex geometries, *IEEE Trans. Plasma Sci.* **23**(4), 769 (1995).

19. S. G. Mason, Fiber motions and flocculation, *Tappi J.* **37**(11), 494 (1954).

20. C. S. Peskin, Flow patterns around heart valves: A numerical method, *J. Comput. Phys.* **10**, 252 (1972).

21. C. S. Peskin, Numerical analysis of blood flow in the heart, *J. Comput. Phys.* **25**, 220 (1977).

22. C. S. Peskin and D. M. McQueen, A three-dimensional computational model for blood flow in the heart. I. Immersed elastic fibers in a viscous incompressible fluid, *J. Comput. Phys.* **81**, 372 (1989).

23. C. S. Peskin and D. M. McQueen, Computational biofluid dynamics, in *Fluid Dynamics in Biology: Proceedings of the AMS-IMS-SIAM Joint Summer Research Conference on Biofluiddynamics, Contemporary Mathematics, Vol. 141*, edited by A. Y. Cheer and C. P. van Dam (Am. Math. Soc. Providence, RI, 1993), p. 161.

24. S. Ranganathan and S. G. Advani, A simultaneous solution for flow and fiber orientation in axisymmetric diverging radial flow, *J. Non-Newton. Fluid Mech.* **47**, 107 (1993).

25. J. Rosenberg, M. Denn, and R. Keunings, Simulations of non-recirculating flows of dilute fiber suspensions, *J. Non-Newton. Fluid Mech.* **37**, 317 (1990).

26. R. F. Ross and D. J. Klingenberg, Dynamic simulation of flexible fibers composed of linked rigid bodies, *J. Chem. Phys.* **106**(7), 2949 (1997).

27. L.-G. Samuelsson, Measurement of the stiffness of fibres, *Svensk Papperstidn.* **66**(15), 541 (1963).

28. J. M. Stockie, *Analysis and Computation of Immersed Boundaries, with Application to Pulp Fibres*, Ph.D. thesis, Institute of Applied Mathematics, University of British Columbia, Vancouver, BC, Canada, 1997.

29. C. A. Stover, D. L. Koch, and C. Cohen, Observations of fibre orientation in simple shear flow of semi-dilute suspensions, *J. Fluid Mech.* **238**, 277 (1992).

30. D. Sulsky and J. U. Brackbill, A numerical method for suspension flow, *J. Comput. Phys.* **96**, 339 (1991).

31. L. Tang and M. C. Altan, Entry flow of fiber suspensions in a straight channel, *J. Non-Newton. Fluid Mech.* **56**, 183 (1995).

32. G. Wherrett, I. Gartshore, M. Salcudean, and J. Olson, A numerical model of fibre motion in shear, in *Proceedings of the 1997 ASME Fluids Engineering Division Summer Meeting, Vancouver, Canada, June 22–26, 1997*.

33. S. Yamamoto and T. Matsuoka, A method for dynamic simulation of rigid and flexible fibers in a flow field, *J. Chem. Phys.* **98**(1), 644 (1993).

34. S. Yamamoto and T. Matsuoka, Viscosity of dilute suspensions of rodlike particles: A numerical simulation method, *J. Chem. Phys.* **100**(4), 3317 (1994).